

Design of Frequency Index Modulated Waveforms for Integrated SAR and Communication on High-Altitude Platforms (HAPs)

Bang Huang, *Graduate Student Member, IEEE*, Sajid Ahmed, *Senior Member, IEEE*,
Mohamed-Slim Alouini, *Fellow, IEEE*,

Abstract—This paper, addressing the integration requirements of radar imaging and communication for High-Altitude Platform Stations (HAPs) platforms, designs a waveform based on linear frequency modulated (LFM) frequency-hopping signals that combines synthetic aperture radar (SAR) and communication functionalities. Specifically, each pulse of an LFM signal is segmented into multiple parts, forming a sequence of sub-pulses. Each sub-pulse can adopt a different carrier frequency, leading to frequency hops between sub-pulses. This design is termed frequency index modulation (FIM), enabling the embedding of communication information into different carrier frequencies for transmission. To further enhance the data transmission rate at the communication end, this paper incorporates quadrature amplitude modulation (QAM) into waveform design. The paper derives the ambiguity function of the proposed waveform and analyzes its Doppler and range resolution, establishing upper and lower bounds for the range resolution. In processing SAR signals, the receiver first removes QAM symbols, and to address phase discontinuities between sub-pulses, a phase compensation algorithm is proposed to achieve coherent processing. For the communication receiver, the user first performs de-chirp processing and then demodulates QAM symbols and FIM index symbols using a two-step maximum likelihood (ML) algorithm. Numerical simulations further confirm the theoretical validity of the proposed approach.

Index Terms—Ambiguity function, Frequency index modulation (FIM), High-Altitude Platform Stations (HAPs), Integrated SAR and communication (ISARAC)

I. INTRODUCTION

THE rapid advancement of high-altitude platforms (HAPs) has unlocked new possibilities for wide-area surveillance, environmental monitoring, and communication applications [1]–[5]. Operating in the stratosphere (approximately 20 km above the ground), HAPs platforms bridge the capabilities of satellites and terrestrial systems, offering the expansive coverage of satellites with the agility and lower latency of ground-based systems [6]. These unique attributes make HAPs ideal for dual-function operations, where both synthetic aperture radar (SAR) imaging [7] and communication [8] are essential. In scenarios such as disaster response, border surveillance, and remote sensing, integrated radar-communication systems deployed on HAPs can significantly enhance situational awareness while enabling real-time data transmission, positioning

HAPs as invaluable assets for both civilian and defense applications [9], [10].

Historically, radar and communication systems on shared platforms have been developed as distinct modules, each with unique signal structures and operational requirements. This separation, however, often leads to inefficiencies in spectrum and power utilization, as well as increased complexity in signal processing and hardware demands [11], [12]. As spectrum resources become increasingly limited, the demand for more efficient and compact systems has become critical. Consequently, achieving seamless integration of radar and communication functions within a single waveform has emerged as a major research priority [13], [14]. This approach seeks to maximize spectral efficiency and minimize hardware redundancy, all while maintaining robust performance for both functionalities [15], [16].

In recent years, hybrid waveform design has emerged as a promising solution to the challenges in integrated sensing and communication (ISAC) systems [17]. By enabling both radar and communication functions within a single waveform, integrated designs enhance resource efficiency and simplify system architecture [18], [19]. Among various waveforms, Orthogonal Frequency Division Multiplexing (OFDM)—widely used in previous mobile communication generations—has garnered considerable research interest for ISAC applications [20]–[26].

Sturm *et al.* [22] conducted extensive simulations with practical parameters, demonstrating the feasibility of OFDM-based ISAC systems. Additionally, [23] investigated the influence of pilot power allocation and positioning on ISAC performance, offering targeted solutions. To mitigate the high peak-to-average power ratio (PAPR) inherent to OFDM signals, [24] and [25] introduced low-PAPR OFDM waveforms using iterative least squares and ADMM-based algorithms, respectively. Moreover, [21], [27], [28] explored combining OFDM with multi-input multi-output (MIMO) technology to form MIMO-OFDM ISAC systems, analyzing their performance benefits. These OFDM-based ISAC advancements are thus positioned to play a pivotal role in next-generation mobile and Wi-Fi communications.

In addition to OFDM, frequency hopping (FH) technology has gained attention for its effective interference avoidance capabilities [29]–[32]. Notably, Wang and Hassanien [31], [32] proposed MIMO ISAC schemes utilizing frequency hopping to transmit information through frequency coding. Building

The authors are with the Computer, Electrical and Mathematical Science and Engineering (CEMSE) division in King Abdullah University of Science and Technology (KAUST), Thuwal 6900, Makkah Province, Saudi Arabia. (Emails: bang.huang@kaust.edu.sa; sajid.ahmed@kaust.edu.sa; slim.alouini@kaust.edu.sa) (Corresponding author: Bang Huang)

on this, [30] combined multi-antenna and frequency hopping techniques to further enhance ISAC system performance. Recently, advanced communication technologies, such as orthogonal time frequency space (OTFS) [20], [33] waveforms and reconfigurable intelligent surfaces (RIS) [34], [34], have also attracted significant research interest for ISAC applications. However, it is essential to recognize that waveform design rooted in communication frameworks can inherently introduce interference, potentially affecting radar performance.

This naturally highlights the potential of radar-specific waveforms for developing integrated sensing and communication (ISAC) or joint radar-communication (RadCom) systems.¹ Widely utilized radar waveforms, such as linear frequency modulated (LFM) and frequency modulated continuous wave (FMCW) signals, are valued for their robustness to Doppler shifts during matched filtering, ability to deliver high range resolution, and improved signal-to-noise ratio through pulse compression. However, traditional LFM and FMCW signals lack the inherent modulation structures necessary for efficient data communication. To address this, researchers have been exploring integrated waveform designs for ISAC that are based on LFM/FMCW signals [35]–[40]. In [37], an approach is proposed that employs amplitude modulation (AM) with FMCW waveforms, enabling communication without compromising radar performance. Meanwhile, [39] presents an ISAC waveform based on multiple phase-shift keying (MPSK) LFM, balancing radar and communication capabilities by evaluating key metrics such as energy leakage, peak-to-side lobe ratio (PSLR), and transmission rate.

Index modulation (IM), a promising technology for next-generation energy-efficient communications, has also been explored for enhancing ISAC. By modulating parameters like phase and frequency within LFM or FMCW waveforms using IM, it is possible to achieve communication with minimal impact on radar performance while improving spectral utilization and transmission rates. For instance, in [38], a frequency IM (FIM)-FMCW waveform is developed, indexing distinct carrier frequencies of FMCW sub-pulses and combining them with amplitude and phase modulation (APM) techniques. Both theoretical and empirical analyses confirm that this method preserves radar detection performance while enhancing communication quality. Moreover, Ma *et al.* [35] integrate IM with sparse arrays and narrowband waveforms, allowing high-resolution radar sensing and superior communication performance with reduced hardware complexity. Additionally, in [36], an innovative ISAC system called multi-carrier agile joint radar communication (MAJoRCom) is proposed based on carrier agile phased array radar (CAESAR). This approach utilizes spatial and spectral agility to enable digital message transmission without sacrificing radar performance, achieving efficient integration of radar and communication functionalities.

In the ISAC solutions discussed above, sensing modules primarily target detection and position estimation. However, as research advances and sensing applications expand, the

ability to generate a comprehensive image of the surrounding environment while supporting communication is gaining significant industry interest [41]–[44]. For example, utilizing HAPs to deliver communication services in remote areas while capturing crop images enables more precise monitoring and management, further promoting the development of intelligent and precision agriculture [1]. Synthetic Aperture Radar (SAR), a widely used radar technology, is increasingly explored for integration into ISAC systems. Notably, OFDM signals have emerged as a focal point of research in SAR imaging applications [45], [46]. In an integrated SAR and communication (ISARAC) framework, Zhang *et al.* proposed using OFDM signal cyclic prefixes (CPs) to enhance SAR imaging and communication capabilities [45]. Additionally, Wang [46] developed an OFDM imaging approach using space-time coding (STC) configurations, which enables range-Doppler signal decoupling and differentiation between communication signals and SAR echoes. Expanding on this, Liu *et al.* [47] introduced a CP-free OFDM-based ISAC system that removes cyclic prefixes to reduce energy loss and mitigate false targets, achieving high-resolution SAR imaging of ground targets while maintaining a low bit error rate (BER) in the communication subsystem. This approach offered detailed analysis and demonstrates superior performance in an air-to-ground scenario. Furthermore, Tan *et al.* introduced an innovative ISARAC architecture that utilizes time-frequency spectrum shaping (TFSS) with short-time Fourier transform (STFT) to embed information and enhance imaging performance, offering a lightweight, low-cost, and secure solution for integrating SAR and communication. Building on this, the same authors [48] later proposed an ISAC waveform design leveraging DFT watermarking to optimize peak sidelobe level (PSL) for covert communication and low probability of interception (LPI) radar sensing, incorporating peak-to-average ratio (PAR) and energy constraints to ensure hardware compatibility, with the approach validated through SAR imaging and communication experiments. Although the aforementioned studies have initiated research on ISARAC, existing work lacks in-depth exploration of practical application scenarios, and the designed waveforms have limited practicality. Therefore, it is essential to further investigate ISARAC waveform design in real-world application contexts to enhance its usability and relevance.

In response to these challenges, this paper proposes a novel integrated waveform based on LFM frequency-hopping (FH-LFM) signals, designed specifically for HAPs platforms to support both SAR imaging and communication. This design, termed FIM, segments each pulse of an LFM signal into sub-pulses, each with a different carrier frequency, effectively creating frequency hops between sub-pulses. By embedding communication data within the frequency indices of these sub-pulses, this approach facilitates simultaneous radar and communication functions. Importantly, the design retains the range resolution advantages of LFM for SAR applications while alleviating the analog-to-digital converter (ADC) sampling requirements, addressing a critical issue in high-resolution radar systems.

The theoretical framework of this waveform includes a detailed derivation of its ambiguity function, allowing an in-

¹RadCom refers to radar technology focused exclusively on sensing, while ISAC integrates radar, vision, and other methods to facilitate sensing.

depth analysis of its Doppler and range resolution characteristics. Upper and lower bounds for range resolution are established to confirm that SAR imaging quality is maintained. To resolve phase discontinuities between sub-pulses, a phase compensation algorithm is introduced, ensuring coherent SAR signal processing. On the communication side, a two-step maximum likelihood (ML) algorithm is employed to demodulate quadrature amplitude modulation (QAM) and frequency index modulation (FIM) symbols, supporting efficient data extraction.

Numerical simulations validate the efficacy of the proposed design, demonstrating that it meets both radar and communication performance requirements. This research presents a significant advancement in the field of HAPs-based integrated radar and communication systems, offering a robust and efficient solution that could enhance the operational capabilities of HAPs platforms in multi-functional scenarios.

The structure of this paper is organized as follows: Section II presents an integrated waveform designed for the ISARAC system and provides an in-depth analysis of its ambiguity function. Section III outlines the design of both the SAR and communication receivers, along with the corresponding algorithms for imaging and demodulation. Following this, numerical simulations, in Section IV are conducted to verify the accuracy and effectiveness of the proposed algorithms. Finally, the conclusions of this paper are summarized in Section V.

II. PROPOSED SIGNAL MODEL OF ISARAC SYSTEM

Consider a scenario in which a HAP at an altitude H travels along a straight path with a constant velocity V as shown in Fig. 1. In this model, we consider a strip-map [49]–[51] HAP that continuously transmits signals for user communication, receives reflected signals from the ground, and strategically combines these received signals to generate an image of the ground. The transmission and reception of SAR signals are both carried out by the HAP, while the transmission and reception of the communication link are handled by the HAP and the user terminal, respectively. To ensure continuous communication with users, the HAP can follow a circular path, or multiple HAPs can be deployed [9]. However, this study focuses solely on a single HAP for SAR imaging at the radar end, and does not address the potential impacts of switching HAPs relays at the communication end.

To achieve both the communication and SAR objectives, mentioned above, we divide a single linear frequency modulated (LFM) pulse into multiple segments, forming a train of sub-pulses. By assigning each sub-pulse a unique frequency band, we implement frequency hopping within the LFM signal to effectively embed communication data. Here, let f_c denote the carrier frequency, B_w the bandwidth, and T_w the pulse width of the LFM signal. The resulting LFM waveform can then be written as:

$$s(t) = p(t)e^{j2\pi(f_c + \frac{1}{2}Kt)t}, \quad (1)$$

where $p(t) = \text{rect}\left(\frac{t}{T_w}\right)$ represents the rectangle function and K is the chirp rate.

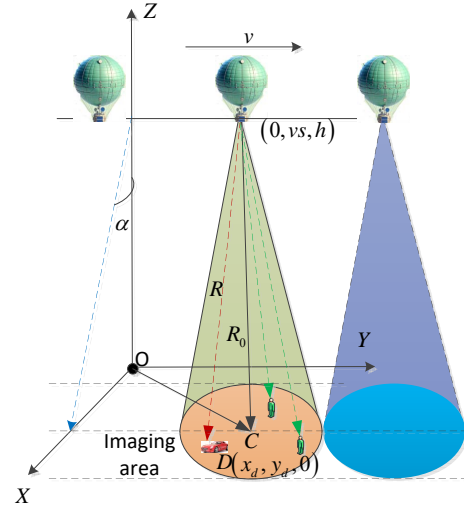


Fig. 1. Basic model of a joint communication and SAR imaging system. The HAP, at an altitude h and traveling along a straight path with velocity v , transmits frequency-modulated sub-pulses, each with a distinct carrier frequency.

Further, we introduce frequency hopping to embed the communication signal into the LFM waveform. For this, LFM chirp can be divided into M sub-chirps, with each sub-chirp having a bandwidth and pulse width that are $\frac{1}{M}$ of the original chirp's bandwidth and duration, respectively, as shown in Fig. 2. Besides, Fig. 2 shows that the entire transmission bandwidth is partitioned into M segments, each with an equivalent bandwidth of B_s . Furthermore, each sub-chirp can transmit any of these segments as needed.

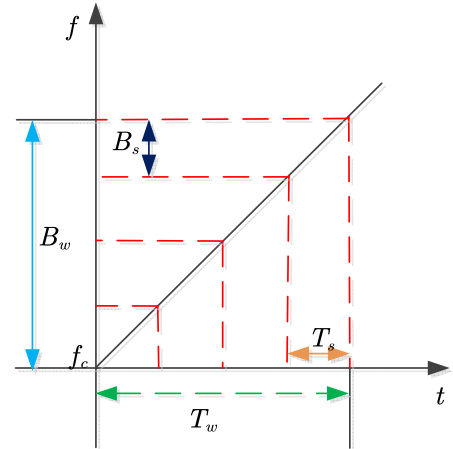


Fig. 2. Illustration for FH-LFM waveform of a chirp on time-frequency domain.

Denote $B_s = \frac{B_w}{M}$, $T_s = \frac{T_w}{M}$, the transmitted signal for m th sub-chirp can be expressed as

$$s_m(t) = p(t - \Delta t_m) \sqrt{P} e^{j2\pi(f_c + a_m B_s + \frac{1}{2}K(t - \Delta t_m))(t - \Delta t_m)}. \quad (2)$$

with $m = 0, 1, \dots, M - 1$ and $\Delta t_m = mT_s$. Further, P stands for the transmit power of ISARAC signal and $a_m \in \{0, 1, 2, \dots, M - 1\}$ is the index of the sub-bandwidth in the

sub-chirp. Therefore, the modulation of the communication signal is achieved by hopping the frequency of the transmitted signal. In fact, the frequency variation of the sub-chirp transmitted signal is accomplished by indexing different signal bandwidths. Hence, this paper designates it as frequency-index modulation (FIM). As provided in Fig. 3, the transmit bits per every pulse is $p_f = M \log_2 M$.

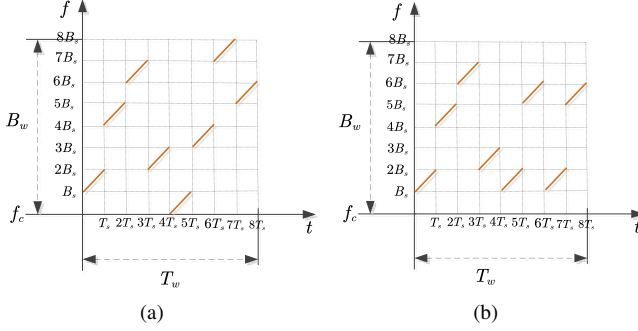


Fig. 3. Examples of FIM-LFM signal of a chirp on time-frequency domain with $M = 8$. (a) $[a_1, a_2, a_3, a_4, a_5, a_6, a_7, a_8] = [1, 4, 6, 2, 0, 3, 7, 5]$. (b) $[a_1, a_2, a_3, a_4, a_5, a_6, a_7, a_8] = [1, 4, 6, 2, 1, 5, 1, 5]$.

Meanwhile, to further enhance the transmission rate of the communication signal, J -QAM will also be utilized. Consequently, a signal incorporating both QAM-FIM modulation and the LFM waveform can be expressed as:

$$s_m(t) = p(t - \Delta t_m) c_m \sqrt{P} \times e^{j2\pi(f_c + a_m B_s + \frac{1}{2}(t - \Delta t_m))(t - \Delta t_m)}. \quad (3)$$

with $c_m = A_m e^{j\phi_m}$ denotes the QAM symbol for the sub-chirp. Note that this paper assumes that A_m and ϕ_m are the amplitude and phase rotation. In this respect, each pulse can carry $p = p_f + M \log_2 J$ bits of communication information.

Moreover, the expression for ISARAC signal consisting of K pulses can be expressed as

$$s(t) = \sum_{k=0}^{K-1} \sum_{m=0}^{M-1} s_{k,m}(t) \quad (4)$$

with the sub-pulse

$$s_{k,m}(t) = p(t - \Delta t_{kM+m}) c_{kM+m} \sqrt{P} \times e^{j2\pi(f_c + a_{kM+m} B_s + \frac{1}{2}K(t - \Delta t_{kM+m}))(t - \Delta t_{kM+m})}. \quad (5)$$

A. Analysis of Ambiguity Function

The ambiguity function of the proposed FIM-LFM waveform can be expressed as:

$$\chi(\tau, \xi) = \int_{-\infty}^{+\infty} \tilde{s}(t) \tilde{s}^*(t + \tau) e^{j2\pi\xi t} dt \quad (6)$$

where τ is the time delay and ξ is the Doppler shift. The transmitted signal over the duration can be written as

$$\tilde{s}(t) = \sum_{m=0}^{M-1} p(t - \Delta t_m) e^{j2\pi(f_c + a_m B_s + \frac{1}{2}K(t - \Delta t_m))(t - \Delta t_m)}. \quad (7)$$

It should be noted that in (7) QAM symbols are not considered. This is because, as detailed in subsequent sections of this paper, QAM symbols are excluded in SAR imaging process. Therefore, their exclusion does not affect the performance of the proposed waveform when applied to SAR images, particularly in the range and Doppler dimensions.

The magnitude of the ambiguity function of $\tilde{s}(t)$ can be derived as

$$|\chi(\tau, \xi)| = (T_s - |\tau|) \text{sinc}(\pi(\xi - K\tau)(T_s - |\tau|)) \times \left| \sum_{m=1}^M e^{j2\pi[\xi m T_s - a_m B_s \tau]} \right|. \quad (8)$$

Please see Appendix A for the proof.

1) *Doppler Resolution*: Inserting $\tau = 0$ in (8) yields the Doppler profile of the ambiguity function as

$$|\tilde{\chi}(0, \xi)| = \left| T_s \text{sinc}(\pi\xi T_s) \frac{\sin(\pi M \xi T_s)}{\sin(\pi \xi T_s)} \right|. \quad (9)$$

Thus, the Doppler resolution of the proposed FIM-LFM waveform is

$$\rho_\xi = \frac{1}{M T_s} = \frac{1}{T_w}, \quad (10)$$

which is consistent with that of the original LFM signal.

2) *Range profile*: Similarly, inserting $\xi = 0$ in (8) results in the range profile of ambiguity function

$$|\tilde{\chi}(\tau, 0)| = \left| (T_s - |\tau|) \text{sinc}(\pi K \tau (T_s - |\tau|)) \times \sum_{m=1}^M e^{-j2\pi a_m B_s \tau} \right|. \quad (11)$$

It should be noted that a_m can change randomly, which makes it challenging to find the range profile. However, we can put a lower and upper bound on the range resolution.

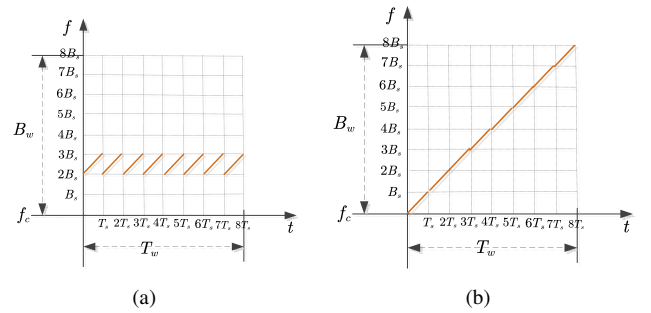


Fig. 4. Examples of FIM-LFM signal of a chirp on time-frequency domain with $M = 8$. (a) $a_m = 2, m = 1, 2, \dots, M$. (b) $a_m = m, m = 1, 2, \dots, M$.

If all sub-pulses choose the same band, as shown in Fig.4(a), it will correspond to the minimum bandwidth of the overall signal. In this case, (11) can be re-written as

$$|\tilde{\chi}(\tau, 0)| = |(T_s - |\tau|) \text{sinc}(\pi K \tau (T_s - |\tau|))|. \quad (12)$$

The range ambiguity function expressed in (12) matches that of an LFM signal with a pulse width T_s and bandwidth B_s and it can be readily derived as

$$\rho_r = \frac{c}{2B_s}, \quad (13)$$

which is an upper bound on the range resolution.

Similarly, for the case when $a_m = m$ shown in Fig.4(b), the spectra of adjacent sub-pulses are continuous. This case will correspond to the maximum bandwidth of the overall signal. Now, the range profile of the ambiguity function can be expressed as

$$|\tilde{\chi}(\tau, 0)| = \left| (T_s - |\tau|) \operatorname{sinc}(\pi K \tau (T_s - |\tau|)) \frac{\sin(\pi M B_s \tau)}{\sin(\pi B_s \tau)} \right|. \quad (14)$$

Using (14) the range resolution of the FIM-LFM signal can be derived as

$$\rho_r = \frac{c}{2M B_s} = \frac{c}{2B_w}, \quad (15)$$

which is the minimum bound on the ambiguity function. In this case, the range resolution of the proposed waveform is consistent with that of the LFM waveform with the pulse width and bandwidth being T_s and B_s , respectively. Therefore, we can say that the range resolution

$$\frac{c}{2B_s} \leq \rho_r \leq \frac{c}{2B_w}. \quad (16)$$

This implies that, due to the frequency hopping of adjacent sub-pulses, the range resolution is no longer a fixed value.

III. RECEIVER DESIGN FOR ISARAC

In this section, we will analyze the SAR and communication receivers of the ISARAC system.

A. SAR receiver

Using (1) the received signal by the SAR can be written as

$$r(t) = \sum_{k=0}^{K-1} \sum_{m=1}^M s_{k,m}(t, \tau(s)), \quad (17)$$

where

$$\begin{aligned} s_{k,m}(t, \tau(s)) &= p(t - \Delta t_{kM+m} - \tau(s)) \sigma c_{kM+m} \\ &\times e^{j2\pi[f_c + a_{kM+m} B_s](t - \Delta t_{kM+m} - \tau(s))} \\ &\times e^{j\pi K(t - \Delta t_{kM+m} - \tau(s))^2}. \end{aligned} \quad (18)$$

while σ denotes the radar cross section (RCS) and $\tau(s)$ represents the time delay experienced by the signal as it travels from the transmitter to the target and then reflects to the SAR receiver. The time delay $\tau(s) = \frac{2R(s)}{c}$ with $R(s)$ representing the range between HAP and the ground scatterer at slow time s can be derived using Fig. 1 as

$$\begin{aligned} R(s) &= \sqrt{x_d^2 + (y_d - vs)^2 + h^2} \\ &\approx R_0 + \frac{(y_d - vs)^2}{2R_0}, \end{aligned} \quad (19)$$

where $R_0 = \sqrt{x_d^2 + h^2}$ is the closest distance between the HAPs and the center of the imaging scene and v denotes the flight speed of the HAPs. Besides, The 3D Cartesian coordinates of the target and the HAPs are represented as $(x_d, y_d, 0)$ and $(0, vs, h)$, respectively. It should be noted that the second approximation in Eq.(19) is obtained through a second-order Taylor expansion.

The received sub-pulse at the SAR receiver after demodulating by the carrier frequency f_c and removing the QAM symbols² can be written as

$$\begin{aligned} \tilde{s}_{k,m}(t, \tau(s)) &= p(t - \Delta t_{kM+m} - \tau(s)) \sigma e^{-j2\pi f_c \tau(s)} \\ &\times e^{j2\pi a_{kM+m} B_s (t - \Delta t_{kM+m} - \tau(s))} \\ &\times e^{j\pi K(t - \Delta t_{kM+m} - \tau(s))^2}. \end{aligned} \quad (20)$$

The phase of the third term will be much less than the first two terms. Therefore, ignoring the phase of the third term, the Doppler frequency of the signal in (20) can be easily obtain:

$$\begin{aligned} f(s) &= \frac{(f_c + a_{kM+m} B_s)(y_d - vs)v}{cR_0} \\ &= \frac{(f_c + a_{kM+m} B_s) y_d v}{cR_0} - \frac{(f_c + a_{kM+m} B_s) v^2 s}{cR_0}. \end{aligned} \quad (21)$$

The presence of the second term in (21) results in a varying signal frequency within a single pulse. Without proper compensation, directly performing azimuth compression is highly likely to cause defocusing of the azimuth signal, preventing the generation of a clear SAR image.

Applying an FFT transform to (20) along the range dimension yields

$$\begin{aligned} S_{k,m}(f_t, \tau(s)) &= \int_{-\infty}^{\infty} \tilde{s}_{k,m}(t, \tau(s)) e^{-j2\pi f_t t} dt \\ &= \sigma p \left[\frac{f_t}{B_s} \right] e^{-j\pi \frac{f_t^2}{K}} e^{-j2\pi(f_c + a_{kM+m} B_s)\tau(s)} \\ &\quad \times e^{-j2\pi f_t (\Delta t_{kM+m} + \tau(s))} \end{aligned}$$

where f_t denoted the range frequency. Furthermore, the following correction factors are introduced for performing pulse compression and time-domain alignment:

$$H_{kM+m}^{rc} = p \left[\frac{f_t}{B_s} \right] e^{-j\pi \frac{f_t^2}{K}} e^{j2\pi f_t \Delta t_{kM+m}} \quad (22)$$

Multiplying the sub-band echo spectrum by (22) to obtain the sub-band spectrum after pulse compression, given as

$$\begin{aligned} S_{k,m}^{rc}(f_t, \tau(s)) &= S_{k,m}(f_t, \tau(s)) H_{kM+m}^{rc} \\ &= \sigma p \left[\frac{f_t}{B_s} \right] e^{-j2\pi(f_c + a_{kM+m} B_s + f_t)\tau(s)} \end{aligned} \quad (23)$$

From (23), it can be seen that each sub-band's frequency is shifted by $a_{kM+m} B_s$. Therefore, to maintain coherence in the azimuth dimension, a shift of $a_{kM+m} B_s$ can be applied in the range frequency dimension. After performing the aforementioned operations, the following is obtained:

$$\begin{aligned} S_{k,m}^{rc}(f_t - a_{kM+m} B_s, \tau(s)) &= \\ \sigma p \left[\frac{f_t - a_{kM+m} B_s}{B_s} \right] e^{-j2\pi(f_c + f_t)\tau(s)} \end{aligned} \quad (24)$$

Next, summing all the sub-pulses of the k th pulse results in

$$\begin{aligned} S_{\text{sum}} &= \sum_{m=1}^M S_{k,m}^{rc}(f_t - a_{kM+m} B_s, \tau(s)) \\ &= \sigma e^{-j2\pi(f_c + f_t)\tau(s)} \sum_{m=1}^M p \left[\frac{f_t - a_{kM+m} B_s}{B_s} \right] \end{aligned} \quad (25)$$

²QAM symbols transmitted by the SAR are known at the SAR receiver.

Next, by transforming the bandwidth-synthesized signal from the range frequency domain into the fast time domain, the following result is obtained:

$$\begin{aligned}
s(t, \tau(s)) &= \int_{-\infty}^{\infty} S_{\text{sum}} e^{j2\pi f_t t} df_t \\
&= \sigma e^{-j2\pi f_c \tau(s)} \sum_{m=1}^M \int_{-\infty}^{\infty} e^{j2\pi f_t (t-\tau(s))} \\
&\quad \times p \left[\frac{f_t - a_{kM+m} B_s}{B_s} \right] df_t \\
&= \sigma e^{-j2\pi f_c \tau(s)} \sum_{m=1}^M \int_{-\frac{B_s}{2} + a_{kM+m} B_s}^{\frac{B_s}{2} + a_{kM+m} B_s} e^{j2\pi f_t (t-\tau(s))} df_t \\
&= \sigma B_s e^{-j2\pi f_c \tau(s)} \text{sinc} [\pi B_s (t - \tau(s))] \\
&\quad \times \sum_{m=1}^M e^{j2\pi a_{kM+m} B_s (t-\tau(s))} \quad (26)
\end{aligned}$$

with $\text{sinc}(x) = \frac{\sin x}{x}$ representing the sinc function.

Hence, this paper proposes the Algorithm 1 to mitigate the impact of intra-pulse chirp on the Doppler frequencies of sub-pulses.

Algorithm 1 Compensation algorithm for echo signal of sub-pulse

- 1: Input the received signal $\tilde{s}_{k,m}(t, \tau(s))$ and a_{kM+m} ;
 - 2: **for** $m = 1$ to M **do**
 - 3: Step 1: Performing FFT to $\tilde{s}_{k,m}(t, \tau(s))$ along range domain yields $S_{k,m}(f_t, \tau(s))$;
 - 4: Step 2: Multiplying the $S_{k,m}(f_t, \tau(s))$ by (22) to obtain $S_{k,m}^{rc}(f_t, \tau(s))$;
 - 5: Step 3: Shifting the sub-band waveforms frequency $a_{kM+m} B_s$ yields $S_{k,m}^{rc}(f_t - a_{kM+m} B_s, \tau(s))$;
 - 6: **end for**
 - 7: Step 4: By summing all the sub-pulse signals of the k pulses and then performing an IFFT transform gives $s(t, \tau(s))$;
 - 8: Output the compensated echo signal.
-

Finally, we can directly employ the Range-Doppler algorithm (RDA) like the operations of range cell migration correction (RCMC) and pulse compression in azimuth dimension to generate SAR images.

B. Communication receiver

The waveform proposed in this paper serves a dual purpose, functioning both as a tool for SAR sensing and as a carrier for communication signals. In this context, we consider an imaging scenario that includes a communication user, assuming the transmitted communication signal propagates through a Line-of-Sight (LOS) channel. Consequently, the received signal at the communication user corresponding to the m th sub-pulse of the k th pulse can be written as:

$$\begin{aligned}
\tilde{s}_{k,m}(t, \tau(s)) &= p(t - \Delta t_{kM+m} - \tau(s)) h_{kM+m} c_{kM+m} \\
&\quad \times \sqrt{P} e^{j2\pi(f_c + a_{kM+m} B_s)(t - \Delta t_{kM+m} - \tau(s))} \\
&\quad \times e^{j\pi K(t - \Delta t_{kM+m} - \tau(s))^2} + n(t), \quad (27)
\end{aligned}$$

where h_{kM+m} denotes the Rayleigh fading channel impulse response, namely $h_{kM+m} \sim \mathcal{N}(0, \sigma^2)$ and $n(t) \sim \mathcal{N}(0, N_o)$ represents the noise at the receiver. Assume that the communication user has the perfect knowledge of the channel and the frame synchronization. If the reference signal known to the user is given by

$$\begin{aligned}
s_{\text{rf}}(t, \tau_{\text{ref}}) &= p(t - \Delta t_{kM+m} - \tau_{\text{ref}}) \\
&\quad \times e^{j2\pi(f_c + \frac{1}{2}K(t - \Delta t_{kM+m} - \tau_{\text{ref}}))(t - \Delta t_{kM+m} - \tau_{\text{ref}})}, \quad (28)
\end{aligned}$$

where $\tau_{\text{ref}} = \frac{R_{\text{ref}}}{c}$ with R_{ref} denoting the closest range between the central point target and the HAPs. The de-chirped signal received for a sub-chirp is expressed as:

$$\begin{aligned}
\tilde{s}_{k,m}(t) &= \tilde{s}_{k,m}(t, \tau(s)) [s_{\text{rf}}(t, \tau_{\text{ref}})]^* \\
&= p(t - \Delta t_{kM+m} - \tau_{\text{ref}}) h_{kM+m} c_{kM+m} \\
&\quad \times \sqrt{P} e^{j2\pi a_{kM+m} B_s (t - \Delta t_{kM+m})} + \tilde{n}(t) \quad (29)
\end{aligned}$$

It should be noted that the terms related to the delay $\tau(s)$ have all been absorbed into h_{kM+m} . Besides, $\tilde{n}(t)$ denotes the noise term.

To demodulate the FIM symbol, we can define a matching filter function as follows:

$$h(a_l) = e^{j2\pi a_l B_s (t - \Delta t_{kM+m})} \quad (30)$$

Subsequently, by correlating the de-chirped signal with multiple matching signals, we derive the results (31), as shown in the top of next page. Furthermore, with the results of (31), the demodulation of a_{kM+m} can be expressed as

$$\hat{a}_{kM+m} = \arg \max_{a_l=0,1,\dots,M-1} \left| \frac{1}{T_s} \int_{-\infty}^{\infty} \tilde{s}_{k,m}^{\text{diff}}(t, a_l) dt \right|^2 \quad (32)$$

By utilizing the detected FIM symbol \hat{a}_{kM+m} , QAM symbol detection can be performed based on the maximum likelihood (ML) approach as follows:

$$\hat{c}_{kM+m} = \arg \min_{c_l \in \mathcal{F}} \left| \tilde{s}_{k,m}^{\text{diff}}(t, \hat{a}_{kM+m}) - h_{kM+m} c_l \sqrt{P} \right|^2 \quad (33)$$

C. Analysis for specific cases

As shown in Eq.(26), the response of the proposed waveform in the fast-time range dimension depends on the sinc function and the summation term related to a_{kM+m} . This section will attempt to analyze the impact of two specific values of a_{kM+m} , as shown in Fig.4, on both the SAR and communication systems.

$$\begin{aligned} \tilde{s}_{k,m}^{\text{diff}}(t, a_l) &= \tilde{s}_{k,m}(t) [h(a_l)]^* \\ &= \begin{cases} p\left(\frac{t-\Delta t_{kM+m}}{T_s}\right) h_{kM+m} c_{kM+m} \sqrt{P} + \tilde{n}(t), & a_l = a_{kM+m} \\ p\left(\frac{t-\Delta t_{kM+m}}{T_s}\right) h_{kM+m} c_{kM+m} \sqrt{P} e^{j2\pi(a_{kM+m}-a_l)B_s(t-\Delta t_{kM+m})}, & a_l \neq a_{kM+m} \end{cases} \end{aligned} \quad (31)$$

1) $a_m = \text{cont.}$: where the symbol cont represents a constant, as shown in Fig.4(a). Under these circumstances, Eq.(26) can be reformulated as:

$$\begin{aligned} s(t, \tau(s)) &= \sigma B_s M e^{-j2\pi[f_c \tau(s) - a_{kM+m} B_s(t-\tau(s))]} \\ &\quad \times \text{sinc}[\pi B_s(t-\tau(s))] \end{aligned} \quad (34)$$

At this point, the response of the waveform proposed in this paper is determined solely by the sinc function in terms of fast-time resolution. Further, the range resolution can be expressed as

$$\rho_r = \frac{c}{2B_s}. \quad (35)$$

Conversely, the transmission of signals with identical frequencies leads to a complete absence of information at the communication end. This occurs because periodic signals inherently lack the capacity to convey any meaningful data.

2) $a_m = m$: This means that the frequency variation between sub-pulses is continuous. Inserting above result into Eq.(26) yields

$$\begin{aligned} s(t, \tau(s)) &= \sigma B_s e^{-j2\pi f_c \tau(s)} \text{sinc}[\pi B_s(t-\tau(s))] \\ &\quad \times \sum_{m=1}^M e^{j2\pi m B_s(t-\tau(s))} \\ &= \sigma B_s e^{-j2\pi f_c \tau(s)} \text{sinc}[\pi B_s(t-\tau(s))] \\ &\quad \times \frac{\sin(\pi M B_s(t-\tau(s)))}{\sin(\pi B_s(t-\tau(s)))} \\ &= \sigma M B_s e^{-j2\pi f_c \tau(s)} \text{sinc}[\pi M B_s(t-\tau(s))] \end{aligned} \quad (36)$$

Therefore, (36) means that the sent signal can be regarded as equivalent to a LFM waveform with a bandwidth of $M B_s$.

Similarly, the highly regular nature of the transmitted waveform results in a significant limitation of the valid information it can carry. From a communications standpoint, such scenarios should be avoided in practical applications. On the other hand, from a SAR perspective, this type of waveform can greatly enhance range resolution. Therefore, in practical implementations, it is crucial to strike a balance between optimizing both SAR and communication functionalities.

IV. SIMULATION RESULTS

To validate the effectiveness of the proposed waveform and corresponding algorithm, this section provides numerical simulation experiments for both SAR and communication systems independently. To elaborate, we assume the carrier frequency of the transmitted signal is 3.2 GHz, with a pulse width of 40 microseconds and a signal bandwidth of 80 MHz. Thus, the range resolution can be expressed as: $\frac{c}{2B} = 1.8750m$. The HAPs has an antenna size of 2 meters in the azimuth direction,

operates at a flight altitude of 20 km, and travels at a speed of 100 m/s. The depression angle with respect to the imaging scene is set at 60° , and the dimensions of the imaging scene are 1000 m by 300 m. In the absence of special instructions, M should be set to 4.

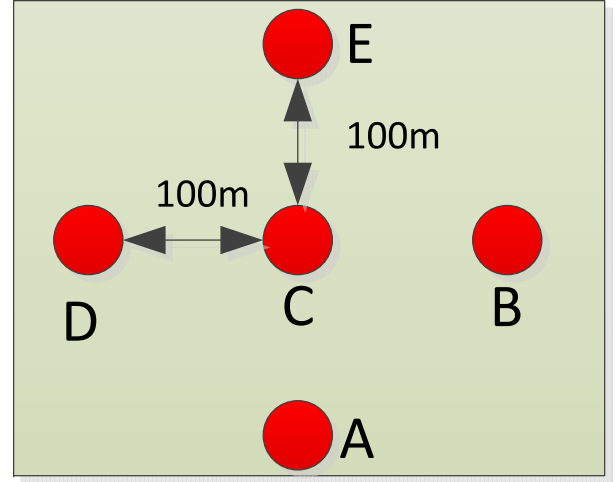


Fig. 5. SAR image depicting a scenario with five distinct point targets.

A. SAR end

As illustrated in Fig. 5, suppose the SAR imaging scene contains five point targets, labeled A, B, C, D, and E. Notably, target C is positioned at the center of the scene, serving as a reference point for the layout.

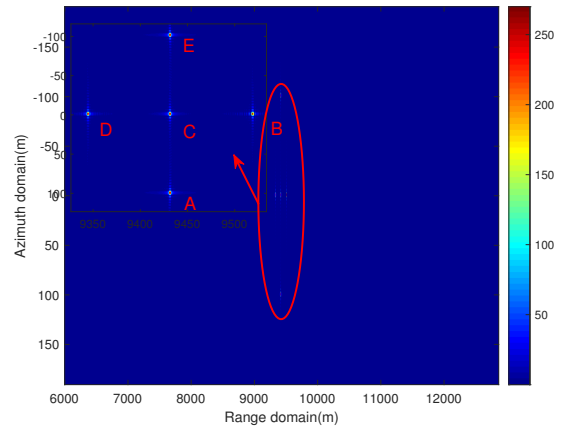
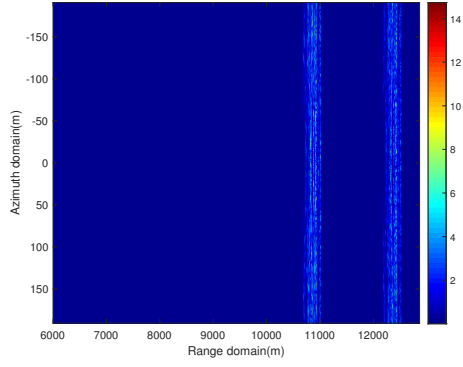
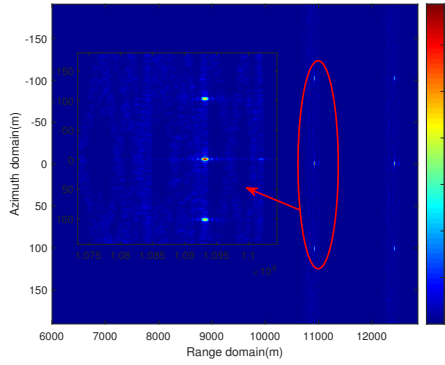


Fig. 6. SAR imaging results obtained using the LFM waveform.

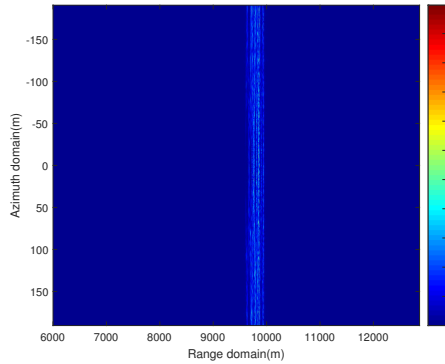
Figures 6 and 7 show SAR images generated using the LFM waveform and the integrated FIM-LFM waveform proposed in



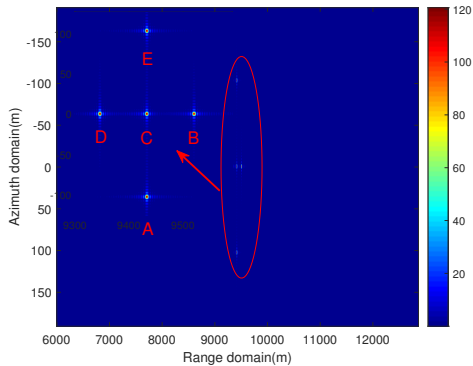
(a) No compensation



(b) After removing QAM symbol



(c) After applying compensation algorithm 1



(d) After removing QAM symbol and applying compensation algorithm 1

Fig. 7. SAR image results by applying our proposed waveform.

this paper, respectively. Fig.7(a) presents the result obtained by directly applying the RD algorithm without removing the QAM symbols or performing Doppler compensation. It can be seen that the SAR image generated by the unprocessed FIM-LFM waveform is severely defocused, and even two strips appear. Further analysis is shown in Fig.7(b), where the result is obtained after removing the QAM symbols embedded in the proposed waveform. At this point, only three of the five pre-set point targets (A, C, and E) in the scene are clearly visible in the SAR image, while the other two targets appear defocused. Additionally, there is still a ghosting issue, as an interference strip identical to the real target appears in the range dimension.

Fig.7(c) shows the SAR image obtained after compensating the FIM-LFM signal for Doppler shifts using only Algorithm 1. Although all targets remain defocused, the number of strips is reduced to one. Finally, by first removing the QAM symbols from the waveform, then using Algorithm 1 to compensate for the Doppler shifts of different sub-pulses, and finally applying the RD algorithm, a well-focused SAR image is obtained, as shown in Fig.7(d). It can be observed that all five pre-set point targets in the scene are clearly displayed in the SAR image.

To further evaluate the advantages and disadvantages of the LFM waveform and the FIM-LFM waveform proposed in this paper in terms of SAR imaging performance, Figures 8 and 9 present magnified images of three randomly selected points (A, B, C) from Figures 6 and 7, respectively. Through comparative analysis of Figures 8 and 9, it can be observed that the main lobe in the range dimension of the SAR image generated using the FIM-LFM waveform proposed in this paper has broadened, indicating a decrease in resolution compared to the SAR targets obtained with the LFM waveform. However, the change in the main lobe in the azimuth dimension is minimal, suggesting that the resolution difference between the two waveforms in the azimuth dimension is not significant.

To further evaluate the advantages and disadvantages of the LFM waveform and the FIM-LFM waveform proposed in this paper in terms of SAR imaging performance, Figures 8 and 9 present magnified images of three randomly selected points (A, B, C) from Figures 6 and 7, respectively. Through comparative analysis of Figures 8 and 9, it can be observed that the main lobe in the range dimension of the SAR image generated using the FIM-LFM waveform has broadened, indicating a decrease in resolution compared to the SAR targets obtained with the LFM waveform. This is also reflected in the range profiles shown in Figures 10 and 11. However, the change in the main lobe in the azimuth dimension is minimal, suggesting that the resolution difference between the two waveforms in the azimuth dimension is not significant. Nonetheless, the azimuth profiles in Figures 12 and 13 indicate variations in the sidelobe depth for targets A and C, which may impact the quality of SAR imaging.

While the above conclusions provide a qualitative analysis, quantitative analysis is introduced to compare the imaging quality differences between the proposed waveform and the LFM waveform using two common metrics in the SAR field: peak sidelobe ratio (PSLR) and integration sidelobe ratio (ISLR). PSLR is defined as the ratio of the highest sidelobe peak value to the main lobe peak value of the point target

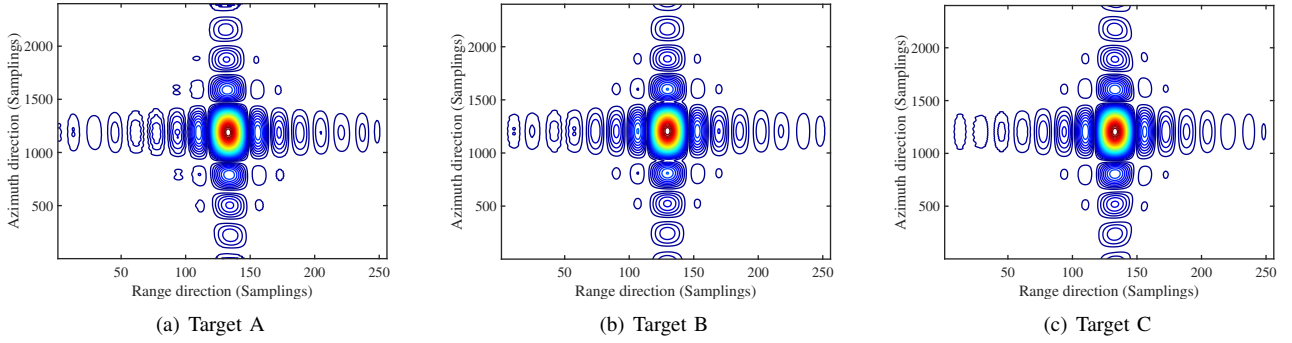


Fig. 8. Magnified image of target for Fig.6.

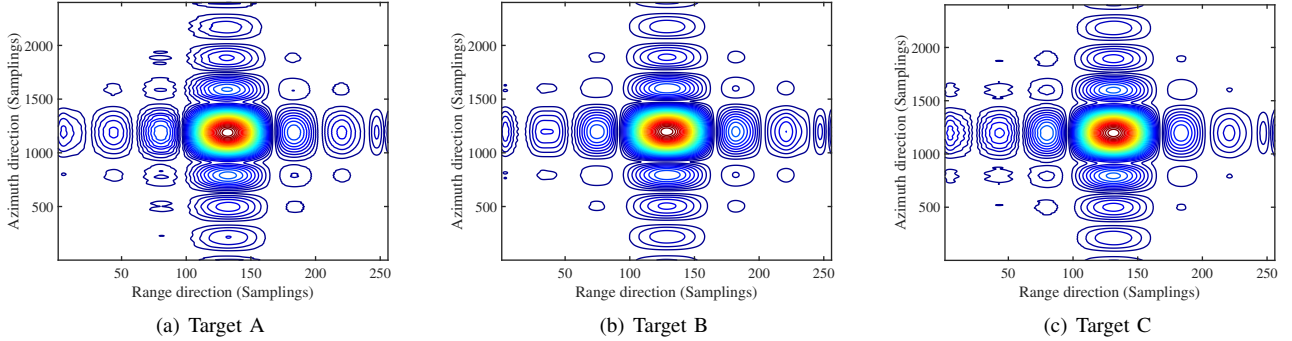


Fig. 9. Magnified image of target for Fig.7.

impulse response, determining the ability of strong targets to "mask" weaker targets. ISLR is defined as the ratio of sidelobe energy to main lobe energy, quantitatively describing the extent to which a locally darker area is "drowned" by energy leakage from surrounding brighter areas. A smaller ISLR value indicates higher image quality. These quantitative metrics provide a basis for further analysis of the differences in imaging quality between the two waveforms. Table I presents the resolution, PSLR, and ISLR assessment results for the three point targets in Figures 8 and 9.

From the table I, it is evident that the range resolution of SAR targets using LFM waveforms closely approaches the ideal resolution, with both ISLR and PSLR metrics showing favorable results. This indicates that the imaging performance of LFM waveforms is quite good. Additionally, as discussed earlier, the SAR target resolution of the proposed method is expected to range between 1.8750 and 7.5000. The results presented in Table 1 further validate the correctness of the earlier theoretical framework. Moreover, the PSLR performance of the two A, C targets in the azimuth dimension has experienced a decline, reinforcing the accuracy of the previous qualitative analysis. It is important to note that the choice of waveform does not influence the azimuth resolution of SAR, as this is primarily determined by the antenna aperture.

The analysis of the magnified images further confirms that the FIM-LFM waveform proposed in this paper experiences some loss of resolution in the range dimension compared to the LFM waveform, but it maintains good performance in the azimuth dimension. This provides valuable insights for the

practical application of the FIM-LFM waveform, especially when considering scenarios that require a balance between communication and other imaging requirements, where the advantages of the FIM-LFM waveform become more apparent.

B. Communication end

Unless stated otherwise, the parameter settings remain consistent with those established earlier. The signal-to-noise ratio (SNR) is defined in decibels (dB) as: $\text{SNR} = 10 \log \frac{P^2}{N_0}$. Besides, set $\sigma^2 = 1$. Moreover, Figure 14 presents the BER performance of the proposed ISARAC system across different QAM modulation orders as a function of SNR. The figure clearly shows that with increasing SNR, the BER decreases, reflecting an enhancement in system performance. Additionally, it is evident that as the modulation order rises, the system transmits more information, but this also leads to a corresponding increase in the error rate. Fig. 15 illustrates the performance of the Bit Error Rate (BER) as a function of Signal-to-Noise Ratio (SNR) under various sub-pulse conditions, with the QAM order set to 4. The graph indicates that as the number of sub-pulses increases, the BER of the proposed system at the communication end tends to rise. This phenomenon can be attributed to the fact that an increase in the number of sub-pulses results in a greater number of bits being transmitted per pulse. For instance, when $M = 2$, the number of transmitted bits is $p = 6$, while for $M = 5$, $p = 20$.

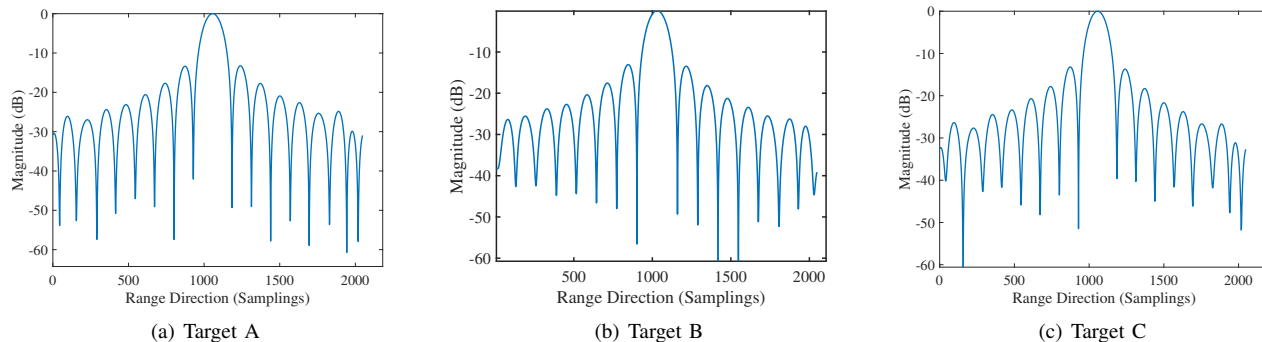


Fig. 10. Range profile for Fig.8.

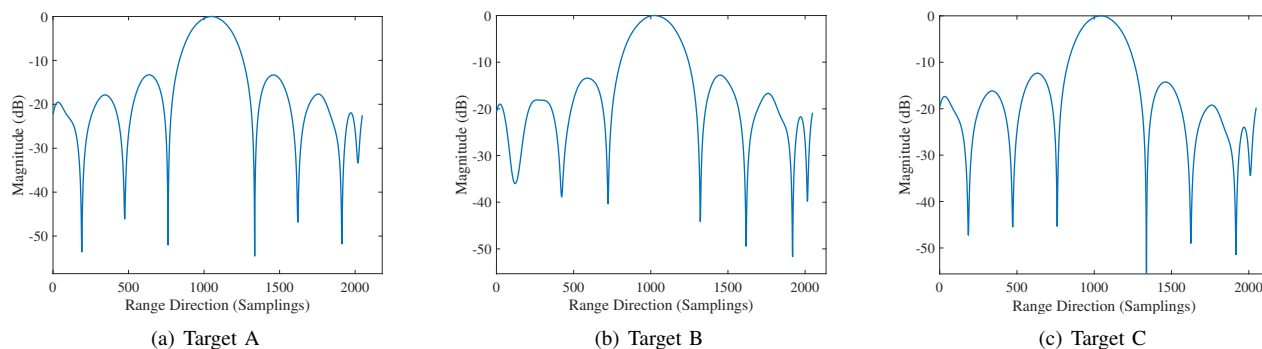


Fig. 11. Range profile for Fig.9.

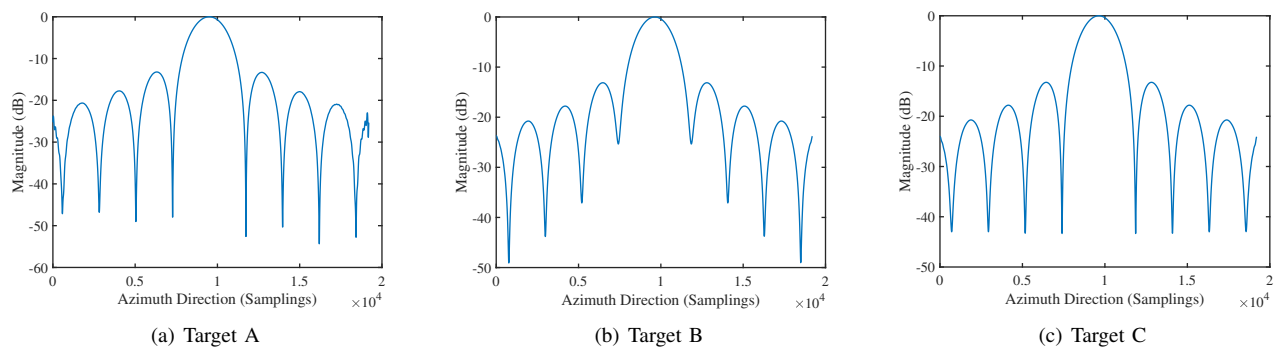


Fig. 12. Azimuth profile corresponding to Fig.8.

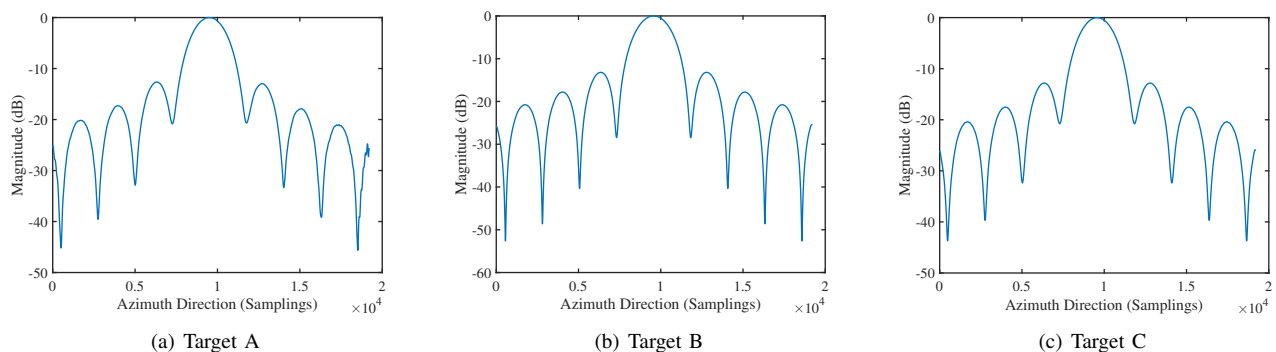


Fig. 13. Azimuth profile corresponding to Fig.9.

TABLE I
EVALUATION OF IMAGING RESULTS

Targets	LFM					
	Range domain			Azimuth domain		
	Resolution(m)	ISLR(dB)	PSLR(dB)	Resolution(m)	ISLR(dB)	PSLR(dB)
Target A	1.8848	-10.2973	-13.2654	3.4759	-10.9346	-13.2654
Target B	1.9013	-10.2907	-13.0704	3.4626	-10.7574	-13.1293
Target C	1.8848	-10.5886	-13.2011	3.4812	-10.9065	-13.2490
Targets	Our proposed waveform					
	Range domain			Azimuth domain		
	Resolution(m)	ISLR(dB)	PSLR(dB)	Resolution(m)	ISLR(dB)	PSLR(dB)
Target A	4.1994	-11.2062	-13.2895	3.5324	-10.4147	-12.6470
Target B	4.3978	-11.0788	-12.7648	3.5200	-10.8710	-13.1981
Target C	4.2325	-10.9507	-12.3531	3.5588	-10.3953	-12.8217

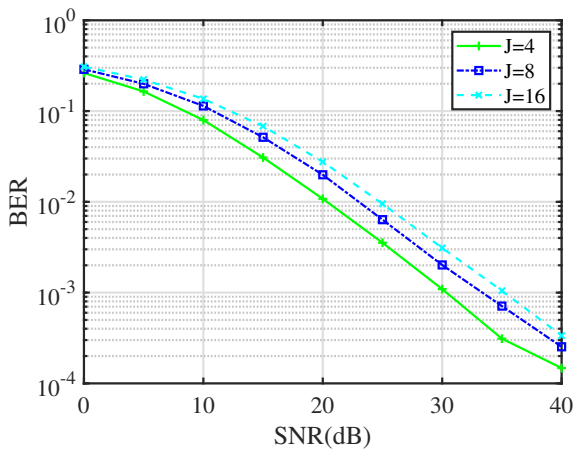


Fig. 14. BER performance by applying our system versus SNR.

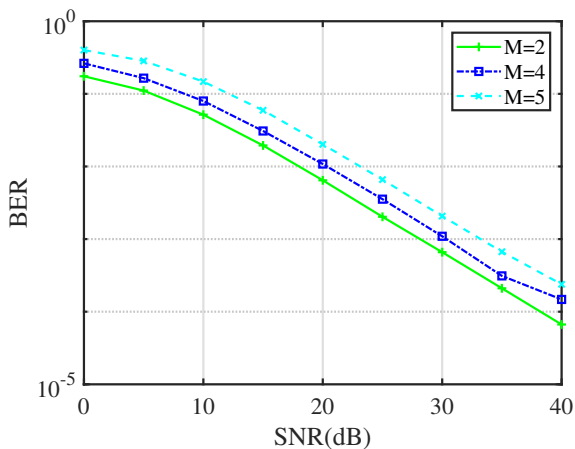


Fig. 15. BER performance by applying our system versus SNR with different sub-pulses.

V. CONCLUSION

This paper presented a novel waveform design for ISARAC on HAPs platforms, based on FIM with LFM frequency-hopping signals. By segmenting each LFM pulse into multiple sub-pulses with distinct carrier frequencies, the proposed approach achieves effective frequency hopping, enabling simultaneous SAR imaging and communication capabilities. This design not only embeds communication information

within varying transmission frequencies but also reduces ADC sampling requirements in the SAR processing chain while preserving range resolution. The derivation of the ambiguity function and analysis of Doppler and range resolution provide a theoretical foundation, with established bounds for range resolution, which further supports the design's effectiveness. Additionally, a phase compensation algorithm is introduced to address phase discontinuities between sub-pulses, ensuring coherent SAR signal processing, while a two-step ML algorithm enables demodulation of QAM and FIM index symbols in the communication receiver. Numerical simulations validate the theoretical analysis and confirm the feasibility and effectiveness of the proposed waveform design, marking a significant step forward in HAPs platform radar-communication integration.

APPENDIX A PROOF OF EQ.(8)

$\chi(\tau, \xi)$ can be further written as

$$\begin{aligned}
 \chi(\tau, \xi) &= P \int_{-\infty}^{+\infty} \sum_{m=1}^M p\left(\frac{t - \Delta t_m}{T_s}\right) \\
 &\quad \times e^{j2\pi(f_c + a_m B_s + \frac{1}{2}K(t - \Delta t_m))(t - \Delta t_m)} \\
 &\quad \times \sum_{m'=1}^M p\left(\frac{t - \Delta t_{m'} + \tau}{T_s}\right) e^{j2\pi\xi t} \\
 &\quad \times e^{-j2\pi(f_c + a_{m'} B_s + \frac{1}{2}K(t + \tau - \Delta t_{m'}))(t + \tau - \Delta t_{m'})} dt \\
 &= P \sum_{m=0}^{M-1} \sum_{m'=0}^{M-1} e^{-j2\pi(f_c + a_{m'} B_s)\tau} \tilde{\chi}(\tau, \xi),
 \end{aligned} \tag{37}$$

where the expression of $\tilde{\chi}(\tau, \xi)$ is

$$\begin{aligned}
 \tilde{\chi}(\tau, \xi) &= \int_{-\infty}^{+\infty} p\left(\frac{t - \Delta t_m}{T_s}\right) p\left(\frac{t + \tau - \Delta t_{m'}}{T_s}\right) \\
 &\quad \times e^{j2\pi f_c(\Delta t_{m'} - \Delta t_m)} e^{j2\pi(a_m - a_{m'})B_s t} e^{j\pi K(t - \Delta t_m)^2} \\
 &\quad \times e^{j2\pi(a_m \Delta t_m - a_{m'} \Delta t_{m'})B_s} e^{-j\pi K(t - \Delta t_{m'} + \tau)^2} e^{j2\pi\xi t} dt.
 \end{aligned} \tag{38}$$

Besides, (37) indicates that $\chi(\tau, \xi)$ consists of the principal term $\tilde{\chi}(\tau, \xi)$ and the coupling term $\bar{\chi}(\tau, \xi)$, namely

$$\chi(\tau, \xi) = \tilde{\chi}(\tau, \xi) + \bar{\chi}(\tau, \xi), \tag{39}$$

with

$$\tilde{\chi}(\tau, \xi) = \sum_{m=0}^{M-1} e^{-j2\pi(f_c + a_m B_s)\tau} \check{\chi}(\tau, \xi), \quad (40)$$

$$\bar{\chi}(\tau, \xi) = b \sum_{m=1}^M \sum_{m'=1, m \neq m'}^M e^{-j2\pi(f_c + a_m B_s)\tau} \check{\chi}(\tau, \xi). \quad (41)$$

The principal term, where $m = m'$, defines the radar's resolution. In contrast, the coupling term, where $m \neq m'$, usually serves as interference and has a lesser impact on resolution. Then we can focus our main efforts on the principal term. In this respect,

$$\begin{aligned} \check{\chi}(\tau, \xi) &= \int_{-\infty}^{+\infty} p\left(\frac{t - \Delta t_m}{T_s}\right) p\left(\frac{t + \tau - \Delta t_m}{T_s}\right) \\ &\quad \times e^{j\pi K(t - \Delta t_m)^2} e^{-j\pi K(t - \Delta t_m + \tau)^2} e^{j2\pi\xi t} dt \\ &= \int_{-\infty}^{+\infty} p\left(\frac{t - \Delta t_m}{T_s}\right) p\left(\frac{t + \tau - \Delta t_m}{T_s}\right) \\ &\quad \times e^{-j\pi K\tau^2} e^{-j\pi K(t - \Delta t_m)\tau} e^{j2\pi\xi t} dt \\ &\stackrel{t = t - \Delta t_m}{=} \int_{-\infty}^{+\infty} p\left(\frac{t}{T_s}\right) p\left(\frac{t + \tau}{T_s}\right) \\ &\quad \times e^{-j\pi K\tau^2} e^{-j2\pi Kt\tau} e^{j2\pi\xi(t - \Delta t_m)} dt. \end{aligned} \quad (42)$$

The expression (42) indicates that different values of τ will affect the limits of integration. To ensure the existence of the integral, the condition $|\tau| < T_s$ must be satisfied. Therefore, we should explore expression (44) based on the different values of τ :

1) *Case 1:* When $0 \leq \tau < T_s$, (42) can be further expressed as

$$\begin{aligned} \check{\chi}(\tau, \xi) &= e^{-j\pi K\tau^2} e^{-j2\pi\xi\Delta t_m} \int_{-\frac{1}{2}T_s}^{\frac{1}{2}T_s - \tau} e^{j2\pi t(\xi - K\tau)} dt \\ &= (T_s - \tau) \operatorname{sinc}[\pi(\xi - K\tau)(T_s - \tau)] \\ &\quad \times e^{-j\pi K\tau^2} e^{-j2\pi\xi\Delta t_m} e^{-j\pi(\xi - K\tau)\tau}. \end{aligned} \quad (43)$$

Moreover, inserting (43) into (40) gives

$$\begin{aligned} \tilde{\chi}(\tau, \xi) &= (T_s - \tau) \operatorname{sinc}[\pi(\xi - K\tau)(T_s - \tau)] \\ &\quad \times \sum_{m=0}^{M-1} e^{-j2\pi(f_c + a_m B_s)\tau} e^{j2\pi\xi m T_s} e^{-j\pi\xi\tau} \end{aligned} \quad (44)$$

2) *Case 2:* If $-T_s < \tau < 0$, we can rewrite (42) as

$$\begin{aligned} \check{\chi}(\tau, \xi) &= e^{-j\pi K\tau^2} e^{-j2\pi\xi\Delta t_m} \int_{-\frac{1}{2}T_s - \tau}^{\frac{1}{2}T_s} e^{j2\pi t(\xi - K\tau)} dt \\ &= (T_s + \tau) \operatorname{sinc}[\pi(\xi - K\tau)(T_s + \tau)] \\ &\quad \times e^{-j\pi K\tau^2} e^{-j2\pi\xi\Delta t_m} e^{-j\pi(\xi - K\tau)\tau}. \end{aligned} \quad (45)$$

Further, applying (45) and (40) results in

$$\begin{aligned} \tilde{\chi}(\tau, \xi) &= (T_s + \tau) \operatorname{sinc}[\pi(\xi - K\tau)(T_s + \tau)] \\ &\quad \times \sum_{m=0}^{M-1} e^{-j2\pi(f_c + a_m B_s)\tau} e^{j2\pi\xi m T_s} e^{-j\pi\xi\tau}. \end{aligned} \quad (46)$$

Next, by combining all the above results, we can obtain expression (8).

REFERENCES

- [1] B. E. Y. Belmekki, A. J. Aljohani, S. A. Althubaity, A. A. Harthi, K. Bean, A. Aijaz, and M.-S. Alouini, "Cellular Network From the Sky: Toward People-Centered Smart Communities," *IEEE Open Journal of the Communications Society*, vol. 5, pp. 1916–1936.
- [2] G. Kurt, M. G. Khoshkholgh, S. Alfattani, A. Ibrahim, T. S. J. Darwish, M. S. Alam, H. Yanikomeroğlu, and A. Yongacoglu, "A Vision and Framework for the High Altitude Platform Station (HAPS) Networks of the Future." [Online]. Available: <http://arxiv.org/abs/2007.15088>
- [3] T. Song, D. Lopez, M. Meo, N. Piovesan, and D. Renga, "High altitude platform stations: the new network energy efficiency enabler in the 6G era," in *2024 IEEE Wireless Communications and Networking Conference (WCNC)*, 2024, pp. 1–6.
- [4] F. A. d'Oliveira, F. C. L. d. Melo, and T. C. Devezas, "High-altitude platforms—present situation and technology trends," *Journal of Aerospace Technology and Management*, vol. 8, no. 3, pp. 249–262, 2016.
- [5] J. Li, J. Paden, C. Leuschen, F. Rodriguez-Morales, R. D. Hale, E. J. Arnold, R. Crowe, D. Gomez-Garcia, and P. Gogineni, "High-altitude radar measurements of ice thickness over the antarctic and greenland ice sheets as a part of operation icebridge," *IEEE Transactions on Geoscience and Remote Sensing*, vol. 51, no. 2, pp. 742–754, 2012.
- [6] D. Renga and M. Meo, "Can high altitude platform stations make 6G sustainable?" *IEEE Communications Magazine*, vol. 60, no. 9, pp. 75–80, 2022.
- [7] W.-Q. Wang and H. Shao, "High altitude platform multichannel SAR for wide-area and staring imaging," *IEEE Aerospace and Electronic Systems Magazine*, vol. 29, no. 5, pp. 12–17, 2014.
- [8] X. Yu, X. Zhang, Y. Rui, K. Wang, X. Dang, and M. Guizani, "Joint resource allocations for energy consumption optimization in HAPS-aided MEC-NOMA systems," *IEEE Journal on Selected Areas in Communications*, pp. 1–1, 2024.
- [9] E. S. Ahrazoglu, I. Altunbas, and E. Erdogan, "Multi-HAPS thz satellite communication: Error and capacity analyses under I/Q imbalance," *IEEE Sensors Journal*, pp. 1–1, 2024.
- [10] S. E. Turk, E. S. Ahrazoglu, E. Erdogan, and I. Altunbas, "Design of energy efficient Multi-HAPS assisted hybrid r/fso satellite communication systems with optimal placement," *IEEE Transactions on Green Communications and Networking*, pp. 1–1, 2024.
- [11] F. Liu and C. Masouros, "A tutorial on joint radar and communication transmission for vehicular networks—part i: Background and fundamentals," *IEEE Communications Letters*, vol. 25, no. 2, pp. 322–326, 2021.
- [12] D. Ma, N. Shlezinger, T. Huang, Y. Liu, and Y. C. Eldar, "Joint radar-communication strategies for autonomous vehicles: Combining two key automotive technologies," *IEEE signal processing magazine*, vol. 37, no. 4, pp. 85–97, 2020.
- [13] M. Bicá and V. Koivunen, "Multicarrier radar-communications waveform design for rf convergence and coexistence," in *ICASSP 2019-2019 IEEE International Conference on Acoustics, Speech and Signal Processing (ICASSP)*. IEEE, 2019, pp. 7780–7784.
- [14] Z. Li, F. Hu, Q. Li, Z. Ling, Z. Chang, and T. Hämäläinen, "Aoi-aware waveform design for cooperative joint radar-communications systems with online prediction of radar target property," *IEEE Transactions on Communications*, vol. 72, no. 10, pp. 6029–6043, 2024.
- [15] J. A. Zhang, F. Liu, C. Masouros, R. W. Heath, Z. Feng, L. Zheng, and A. Petropulu, "An overview of signal processing techniques for joint communication and radar sensing," *IEEE Journal of Selected Topics in Signal Processing*, vol. 15, no. 6, pp. 1295–1315, 2021.
- [16] A. Chakravarthi Mahipathi, B. Pardhasaradhi, P. Lingadevaru, P. Srihari, J. D'Souza, and L. Reddy Cenkeramaddi, "A survey on waveform design for radar-communication convergence," *IEEE Access*, vol. 12, pp. 75 442–75 461, 2024.
- [17] H. Ma, "Integrated sensing and communication - the ISAC technology," in *2024 IEEE 2nd International Conference on Sensors, Electronics and Computer Engineering (ICSECE)*, 2024, pp. 225–229.
- [18] Y. Liu, G. Liao, J. Xu, Z. Yang, and Y. Zhang, "Adaptive OFDM integrated radar and communications waveform design based on information theory," *IEEE Communications Letters*, vol. 21, no. 10, pp. 2174–2177, 2017.
- [19] Z. Xiao and Y. Zeng, "Waveform design and performance analysis for full-duplex integrated sensing and communication," *IEEE Journal on Selected Areas in Communications*, vol. 40, no. 6, pp. 1823–1837, 2022.
- [20] L. Gaudio, M. Kobayashi, B. Bissinger, and G. Caire, "Performance analysis of joint radar and communication using ofdm and ofts," in *2019 IEEE International Conference on Communications Workshops (ICC Workshops)*. IEEE, 2019, pp. 1–6.

- [21] Z. Xiao, R. Liu, M. Li, Q. Liu, and A. L. Swindlehurst, "A novel joint angle-range-velocity estimation method for MIMO-OFDM ISAC systems," *IEEE Transactions on Signal Processing*, 2024.
- [22] C. Sturm, T. Zwick, and W. Wiesbeck, "An ofdm system concept for joint radar and communications operations," in *VTC Spring 2009-IEEE 69th Vehicular Technology Conference*. IEEE, 2009, pp. 1–5.
- [23] H.-W. Hsu, M.-C. Lee, M.-X. Gu, Y.-C. Lin, and T.-S. Lee, "Analysis and design for pilot power allocation and placement in OFDM based integrated radar and communication in automobile systems," *IEEE Transactions on Vehicular Technology*, vol. 71, no. 2, pp. 1519–1535, 2021.
- [24] T. Huang and T. Zhao, "Low pmep ofdm radar waveform design using the iterative least squares algorithm," *IEEE Signal Processing Letters*, vol. 22, no. 11, pp. 1975–1979, 2015.
- [25] J. Wu, L. Li, W. Lin, J. Liang, and Z. Han, "Low-complexity waveform design for papr reduction in integrated sensing and communication systems based on ADMM," *IEEE Sensors Journal*, 2024.
- [26] F. Liu, Y. Zhang, Y. Xiong, S. Li, W. Yuan, F. Gao, S. Jin, and G. Caire, "OFDM achieves the lowest ranging sidelobe under random ISAC signaling," *arXiv preprint arXiv:2407.06691*, 2024.
- [27] Z. Wei, J. Piao, X. Yuan, H. Wu, J. A. Zhang, Z. Feng, L. Wang, and P. Zhang, "Waveform design for mimo-ofdm integrated sensing and communication system: An information theoretical approach," *IEEE Transactions on Communications*, 2023.
- [28] P. Li, M. Li, R. Liu, Q. Liu, and A. L. Swindlehurst, "MIMO-OFDM ISAC waveform design for range-doppler sidelobe suppression," *arXiv preprint arXiv:2406.17218*, 2024.
- [29] A. K. Boroujeni, G. Bagheri, and S. Köpsell, "Enhancing frequency hopping security in isac systems: A physical layer security approach," in *2024 IEEE 4th International Symposium on Joint Communications & Sensing (JC&S)*. IEEE, 2024, pp. 1–6.
- [30] K. Wu, J. A. Zhang, X. Huang, and Y. J. Guo, "Frequency-hopping MIMO radar-based communications: An overview," *IEEE Aerospace and Electronic Systems Magazine*, vol. 37, no. 4, pp. 42–54, 2021.
- [31] X. Wang and J. Xu, "Co-design of joint radar and communications systems utilizing frequency hopping code diversity," in *2019 IEEE Radar Conference (RadarConf)*. IEEE, 2019, pp. 1–6.
- [32] A. Hassaniien, B. Himed, and B. D. Rigling, "A dual-function MIMO radar-communications system using frequency-hopping waveforms," in *2017 IEEE Radar Conference (RadarConf)*. IEEE, 2017, pp. 1721–1725.
- [33] W. Yuan, Z. Wei, S. Li, R. Schober, and G. Caire, "Orthogonal time frequency space modulation—part iii: ISAC and potential applications," *IEEE Communications Letters*, vol. 27, no. 1, pp. 14–18, 2022.
- [34] Q. Zhu, M. Li, R. Liu, and Q. Liu, "Joint transceiver beamforming and reflecting design for active RIS-aided ISAC systems," *IEEE Transactions on Vehicular Technology*, vol. 72, no. 7, pp. 9636–9640, 2023.
- [35] D. Ma, N. Shlezinger, T. Huang, Y. Liu, and Y. C. Eldar, "FRaC: FMCW-based joint radar-communications system via index modulation," *IEEE journal of selected topics in signal processing*, vol. 15, no. 6, pp. 1348–1364, 2021.
- [36] T. Huang, N. Shlezinger, X. Xu, Y. Liu, and Y. C. Eldar, "MAJoRCom: A dual-function radar communication system using index modulation," *IEEE Transactions on signal processing*, vol. 68, pp. 3423–3438, 2020.
- [37] P. Barrenechea, F. Elferink, and J. Janssen, "FMCW radar with broadband communication capability," in *2007 European Radar Conference*. IEEE, 2007, pp. 130–133.
- [38] M.-X. Gu, M.-C. Lee, Y.-S. Liu, and T.-S. Lee, "Design and analysis of frequency hopping-aided FMCW-based integrated radar and communication systems," *IEEE Transactions on Communications*, vol. 70, no. 12, pp. 8416–8432, 2022.
- [39] R. Xie, K. Luo, and T. Jiang, "Waveform design for LFM-MPSK-based integrated radar and communication toward IoT applications," *IEEE Internet of Things Journal*, vol. 9, no. 7, pp. 5128–5141, 2021.
- [40] D. Ma, N. Shlezinger, T. Huang, Y. Shavit, M. Namer, Y. Liu, and Y. C. Eldar, "Spatial modulation for joint radar-communications systems: Design, analysis, and hardware prototype," *IEEE Transactions on Vehicular Technology*, vol. 70, no. 3, pp. 2283–2298, 2021.
- [41] Z. Liu, F. Zesong, P. Liu, X. Wang, Z. Zheng, D. Zhou, and W. Yuan, "Integrated sensing and communication for UAV-Borne SAR systems," in *2023 22nd International Symposium on Communications and Information Technologies (ISCIT)*. IEEE, 2023, pp. 1–6.
- [42] M. Manzoni, S. Moro, F. Linsalata, M. G. Polisano, A. V. Monti-Guarnieri, and S. Tebaldini, "Evaluation of UAV-Based ISAC SAR imaging: Methods and performances," in *2024 IEEE Radar Conference (RadarConf24)*. IEEE, 2024, pp. 1–6.
- [43] M.-A. Lahmeri, W. Ghanem, C. Knill, and R. Schober, "Trajectory and resource optimization for UAV synthetic aperture radar," in *2022 IEEE Globecom Workshops (GC Wkshps)*. IEEE, 2022, pp. 897–903.
- [44] M.-A. Lahmeri, V. Mustieles-Pérez, M. Vossiek, G. Krieger, and R. Schober, "UAV formation and resource allocation optimization for communication-assisted 3D InSAR sensing," *arXiv preprint arXiv:2407.06607*, 2024.
- [45] T. Zhang and X.-G. Xia, "OFDM synthetic aperture radar imaging with sufficient cyclic prefix," *IEEE Transactions on Geoscience and Remote Sensing*, vol. 53, no. 1, pp. 394–404, 2014.
- [46] J. Wang, X.-D. Liang, L.-Y. Chen, L.-N. Wang, and K. Li, "First demonstration of joint wireless communication and high-resolution SAR imaging using airborne MIMO radar system," *IEEE Transactions on Geoscience and Remote Sensing*, vol. 57, no. 9, pp. 6619–6632, 2019.
- [47] G. Liu, Y. Wang, and W. Yang, "Radar sensor and data communication system based on OFDM without cyclic prefix," *IEEE Sensors Journal*, vol. 23, no. 7, pp. 7578–7590, 2022.
- [48] J. Yang, Y. Tan, X. Yu, G. Cui, and D. Zhang, "Waveform design for watermark framework based DFRC system with application on joint SAR imaging and communication," *IEEE Transactions on Geoscience and Remote Sensing*, vol. 61, pp. 1–14, 2023.
- [49] M. Jirousek, M. Peichl, S. Anger, S. Dill, and M. Limbach, "The DLR high altitude platform synthetic aperture radar instrument HAPSAR," in *EUSAR 2024; 15th European Conference on Synthetic Aperture Radar*, 2024, pp. 1244–1248.
- [50] M. Jirousek, M. Peichl, S. Anger, M. Engel, S. Dill, R. Scheiber, and S. Baumgartner, "Synthetic aperture radar design for a high-altitude platform," in *EUSAR 2022; 14th European Conference on Synthetic Aperture Radar*, 2022, pp. 1–4.
- [51] M. Jirousek, M. Peichl, S. Anger, S. Dill, and M. Engel, "Design of a synthetic aperture radar instrument for a high-altitude platform," in *IGARSS 2023 - 2023 IEEE International Geoscience and Remote Sensing Symposium*, 2023, pp. 2045–2048.